# Impacts of Auroral Precipitation on HF Propagation: A Hypothetical Over-the-Horizon Radar Case Study

Joshua James Ruck[1] and David R. Themens[1]

[1]University of Birmingham

November 22, 2022

## Abstract

Over-the-horizon radar (OTHR) systems operating in the high-frequency (HF) band (3-30MHz) are unique in their ability to detect targets at extreme ranges, offering cost-effective large area surveillance. Due to their reliance on the reflective nature of the ionosphere in this band, OTHR systems are extremely sensitive to ionospheric conditions and can expect significant variations in operational performance. At high latitudes, the presence of auroral enhancements in the E-Region electron density can substantially modify the coverage area and frequency management of OTHR systems. In this study, HF raytracing is utilized to investigate these impacts for a hypothetical radar under different auroral conditions simulated using the Empirical Canadian High Arctic Ionospheric Model (E-CHAIM). Aurora were seen to increase maximum useable frequency (MUF) from 8.5 MHz to 26 MHz whilst also reducing median available target range from 2541 km to 1226 km, for the greatest differences. Target interception showed large variations in path coverage of between 33-115% and 0-107% for two flight paths tested with precipitation toggled. Two distinct propagation modes were observed with aurora, noted as the F-E ducted and Auroral E-modes. Long-range coverage provided by the auroral F-E ducted mode was of limited capacity with low solar activity due to the reduced NmF2. F-mode propagation transitioned to the dominating Auroral E-mode between Auroral Electrojet (AE) index values of 50- and 200-nT. The significant variations in both frequency and coverage observed within this study highlight some aspects of the importance of considering aurora in OTHR modelling and design.

## Hosted file

`essoar.10507926.1.docx` available at https://authorea.com/users/536189/articles/598980-impacts-of-auroral-precipitation-on-hf-propagation-a-hypothetical-over-the-horizon-radar-case-study

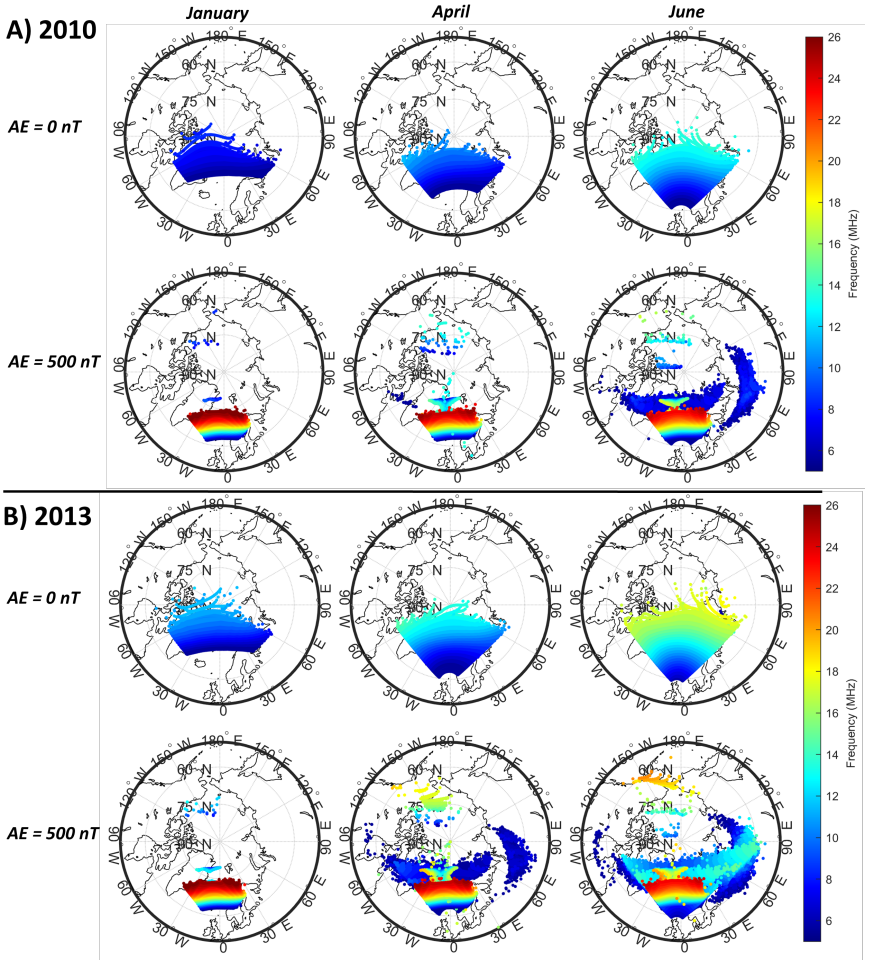

Joshua Ruck[1], David R. Themens[1,2]

[1] Space Environment and Radio Engineering (SERENE) Group, School of Engineering, University of Birmingham, Birmingham, UK

[2] Department of Physics, University of New Brunswick, Fredericton, NB, Canada

Key Points:

1) Auroral conditions associated with AE index > 100nT substantially modify the coverage of a hypothetical OTHR in northern UK

2) Enhanced auroral activity causes a significant decrease in the coverage area of a northern UK OTHR system and an increase in overall MUF

3) In instances of low background electron density, such as solar minimum winter, aurora may be the only available mode for OTHR operation

# Abstract

Over-the-horizon radar (OTHR) systems operating in the high-frequency (HF) band (3-30MHz) are unique in their ability to detect targets at extreme ranges, offering cost-effective large area surveillance. Due to their reliance on the reflective nature of the ionosphere in this band, OTHR systems are extremely sensitive to ionospheric conditions and can expect significant variations in operational performance. At high latitudes, the presence of auroral enhancements in the E-Region electron density can substantially modify the coverage area and frequency management of OTHR systems. In this study, HF raytracing is utilized to investigate these impacts for a hypothetical radar under different auroral conditions simulated using the Empirical Canadian High Arctic Ionospheric Model (E-CHAIM). Aurora were seen to increase maximum useable frequency (MUF) from 8.5 MHz to 26 MHz whilst also reducing median available target range from 2541 km to 1226 km, for the greatest differences. Target interception showed large variations in path coverage of between 33-115% and 0-107% for two flight paths tested with precipitation toggled. Two distinct propagation modes were observed with aurora, noted as the F-E ducted and Auroral E-modes. Long-range coverage provided by the auroral F-E ducted mode was of limited capacity with low solar activity due to the reduced NmF2. F-mode propagation transitioned to the dominating Auroral E-mode between Auroral Electrojet (AE) index values of 50- and 200-nT. The significant variations in both frequency and coverage observed within this study highlight some aspects of the importance of considering aurora in OTHR modelling and design.

## Plain Language Summary

Over-the-horizon radar (OTHR) systems can detect targets at extreme ranges by reflecting high-frequency radio waves in the 3-30MHz band off the ionosphere, an ionised portion of the upper atmosphere, to beyond the horizon. Due to the large coverage area provided by a single radar, OTHR can be a cost-effective solution to monitoring expansive areas; however, as OTHR relies on the ionosphere to reflect radio waves, any disturbances that may be present within the ionosphere, such as aurora, can have a profound effect on the operation of OTHR systems. This may be realised as a drastic change in available coverage area and a disruption to operational frequency, amongst other effects. To better understand the direct implications of aurora on OTHR operation, we model a hypothetical OTHR using specialised computer code to represent the ionosphere and trace the path of radio waves under different conditions. We find that principally, aurora act to increase the maximum frequency available to the radar whilst also reducing the overall range of the covered area. In addition to this, we observed aurora reflecting radio waves in two new manners, unavailable without aurora present; this included the ducting of radio waves and the introduction of lower altitude reflections.

## Introduction

Over-the-horizon Radar (OTHR) systems can detect targets at ranges far exceeding the typical ground level radar horizon, in some cases exceeding 3500 km (Thayaparan et al., 2017). For comparison, the radar horizon for a 20 km altitude target tracked by a 10 m high radar is only 583.11 km (Doerry, A. W., 2013). This over-the-horizon capability is achieved by a unique property of the ionosphere, an ionized region of the upper atmosphere, whereby this region has the capacity to reflect radio waves in the HF range. This allows transmitted signals to 'skip' between the ionosphere and surface before being reflected by a target back to a receiver. Reflection is dependent on transmission frequency, elevation angle, and the refractive index of the ionosphere. For the simplified case whereby particle collisions and Earth's magnetic field are ignored, refractive index can be reduced to the following (Davies, 1965):

$$\mu^2 = 1 - 81\frac{\mathrm{N}}{f^2} \#1$$

where $\mu$ is the real refractive index, $N$ is the electron density and $f$ is the wave frequency. From this, Snell's law predicts that for a given frequency and elevation angle $\theta$, reflection will occur given an electron density of (Riddolls, 2006):

$$N = \frac{f^2 \sin^2\theta}{81} \#2$$

Further accommodations can be made to account for curved geometries as well [Smith, 1939]. It can be deduced from Equation 2 that it is possible to reflect higher frequency rays at lower elevation angles. The critical frequency at vertical incidence (foF2) gives a meaningful indication of the state of the ionosphere and can be readily obtained experimentally using ionosondes or via ionospheric models. foF2 is related to the maximum density of the ionosphere such that

$$foF2 = 9\sqrt{N_{\max}} \ \#3$$

where $N_{max}$ is the maximum density of the ionosphere in electrons per cubic metre. The maximum usable frequency (MUF) is widely used within the radio community to describe the availability of the ionosphere for HF propagation, as higher frequencies are limited by the peak electron density. In operation, OTHR systems are susceptible to significant variations in coverage and detection performance due to their dependence on reflection by the ionosphere (Cervera et al., 2018). At mid latitudes, these variations are mainly dominated by climatological variations in the ionosphere's electron density, large scale responses to geomagnetic activity, and travelling ionospheric disturbances (TIDs) (Cervera & Harris, 2014). At high latitudes however, this problem is worsened by aurora and other complex geomagnetic processes, which can substantially complicate the variability and dynamics of the ionosphere. Furthermore, the low background ionospheric densities in these regions substantially limit the range of viable operable frequencies that can be sustained by F-Region propagation, and the significant variability of this density can require very dynamic frequency management. This is further complicated at night, where increased particle precipitation can dramatically increase the plasma density in the E-region (80- to 150-km in altitude), marked by an enhancement in NmE (the E-Region peak density). Due to significant temporal and spatial fluctuations in the plasma density and the presence of auroral structures, the propagation of HF radio waves within this region can often be unexpected (Hunsucker & Bates, 1969). Because of these complexities, it is essential to evaluate the propagation environment prior to and during deployment so that target detection is accurate and reliable.

OTHR systems make use of a Frequency Monitoring System (FMS) to select feasible radar parameters for the immediate ionospheric conditions. Several studies by Francis et al. (2017), Cervera et al. (2018), Thayaparan et al. (2016, 2018, 2019, 2020) and Chengyu et al. (2015) have previously investigated feasible radar parameters to explore hypothetical OTHR deployments in varied locations, including at high latitudes. Initial attempts by Thayaparan et al. (2016, 2017, 2018, 2019) have been disadvantaged by limitations in the widely used International Reference Ionosphere (IRI) model used to represent electron density; studies by Themens et al. (2014, 2016) and Bjoland et al. (2016) have shown the IRI to perform poorly within the arctic region, with deviations of up to 80% for total electron content (TEC), the column integrated electron density of the ionosphere (Themens & Jayachandran, 2016). The Empirical Canadian

High Arctic Ionospheric Model (E-CHAIM) was developed to address this issue, offering up to 60% improvements in NmF2 over the IRI (Themens et al., 2017). Thayaparan et al. (2020) made use of E-CHAIM in a revised study but included no explicit consideration to aurora, despite their significance to OTHR operating in the arctic. Recently, Mingalev et al. [2021] have assessed the difference in propagation behaviour between the IRI and their Global Dynamic Model of the Ionosphere (GDMI), noting that GDMI's accounting for some portion of the auroral enhancement in the E-Region could account for some of the observed differences in propagation between the two models; however, comprehensive assessment of the impact of aurorally enhanced E-Region density was not conducted and no controls were enacted to isolate this impact, as it was not a principal focus of that study. Unaffected by limitations in the IRI, Francis et al. (2017) and Cervera et al. (2018) demonstrated a comprehensive methodology for modelling the performance of hypothetical OTHR situated in New Zealand. Cervera et al. (2018) used the Australian Defence Science and Technology Organisation (DSTO)-developed PHaRLAP numerical raytracing (NRT) package for their study (Cervera M., 2021), whilst Thayaparan et al. (2016, 2018, 2019, 2020) instead used a custom 3D NRT package.

Raytracing is a technique used to determine the propagation path of HF radio waves through the ionosphere and has been widely used for many decades. Haselgrove (1960, 1963) derived the Hamiltonian equations of geometrical optics to describe radio waves propagating through the ionosphere, and this result has formed the basis of numerous NRT studies (Croft, 1967; Jones & Stephenson, 1975; Settimi & Bianchi, 2014).

Due to their cost-effective application to large area airspace surveillance, OTHRs provide a favourable solution for monitoring airspace over vast regions such as the arctic. The Canadian Department of National Defence (DND) have long pursued HF radar technology since 1984 to monitor the nation's expansive coastline, resulting in two operational HF Surface-Wave Radar (HFSWR) installations (Riddolls, 2006). HFSWR systems offer reduced range in comparison to skywave OTHR, up to only ~370 km, and are only suitable for tracking large ships at sea due to the limited azimuthal accuracy they offer (Ponsford, 2015). Furthermore, the presence of significant ground clutter restricts the use of HFSWR for tracking airborne targets over land, and due to this, recent efforts by most nations have been focussed on maturing skywave OTHR technologies. The Australian Jindalee Operational Radar Network (JORN) is an example of a highly matured and integrated OTHR system currently in operation, realised by many years of HF radar research and investment (Cameron, 1995). With the arctic slowly opening to increased activity from many countries (Nengye Liu, 2017), one could imagine the surveillance benefits that could be achieved by operating an OTHR system within the UK to monitor this region. Whilst no OTHR is currently in operation within the UK, a previous deployment in the late 1960s was attempted under the name Cobra Mist, but due to an undetermined noise source, operational classification was never achieved (Fowle, Key, Millar, & Sear, 1979).

In this study, the effects of aurora on OTHR propagation, specifically the propagation modes afforded by them, will be assessed for a hypothetical OTHR system deployed to northern UK. System coverage and target interception are assessed. A propagation model for the hypothetical radar is demonstrated using E-CHAIM and the PHaRLAP raytracing toolbox to extract frequency and elevation angle of rays intercepting a 10 km target altitude. The modelled impacts are assessed with respect to solar cycle, season, and geomagnetic disturbance level. From this study, the range and sensitivity of operating parameters obtained herein will help guide future high latitude OTHR developments to be aurora tolerant. This will be assessed through four main analysis situations: 1) a coverage analysis test, where the frequency coverage of the system will be assessed in section 3.1, 2) a propagation sensitivity analysis, where boresight coverage will be tested in section 3.2 for a range of geomagnetic disturbance levels, 3) a target intercept analysis, where system interception of example flights will be assessed in section 3.3, and 4) a case study during a moderate geomagnetic storm in May, 2010 presented in section 3.4.

# Methodology and Propagation Model

## Hypothetical OTH radar setup

To explore auroral effects on high-frequency (HF) radar propagation and coverage, a hypothetical OTHR deployment was envisioned to form the basis of this investigation. The model radar was located at Inverness, Scotland (57°42'N 3°20'W) as shown in Figure 1 with an azimuthal coverage of 90° and north facing boresight. With this arrangement, the speculated coverage area for single hop propagation directly intersected the auroral zone. The hypothetical OTHR was tasked with long-range airspace monitoring of commercial air traffic. The red circles in Figure 1 indicate 500- to 3,500-km range markings for the notional range of the radar. For comparison, the 470 km range of a hypothetical co-located Lockheed-Martin TPS-77 long-range surveillance radar (Lockheed-Martin, 2021) is illustrated to show

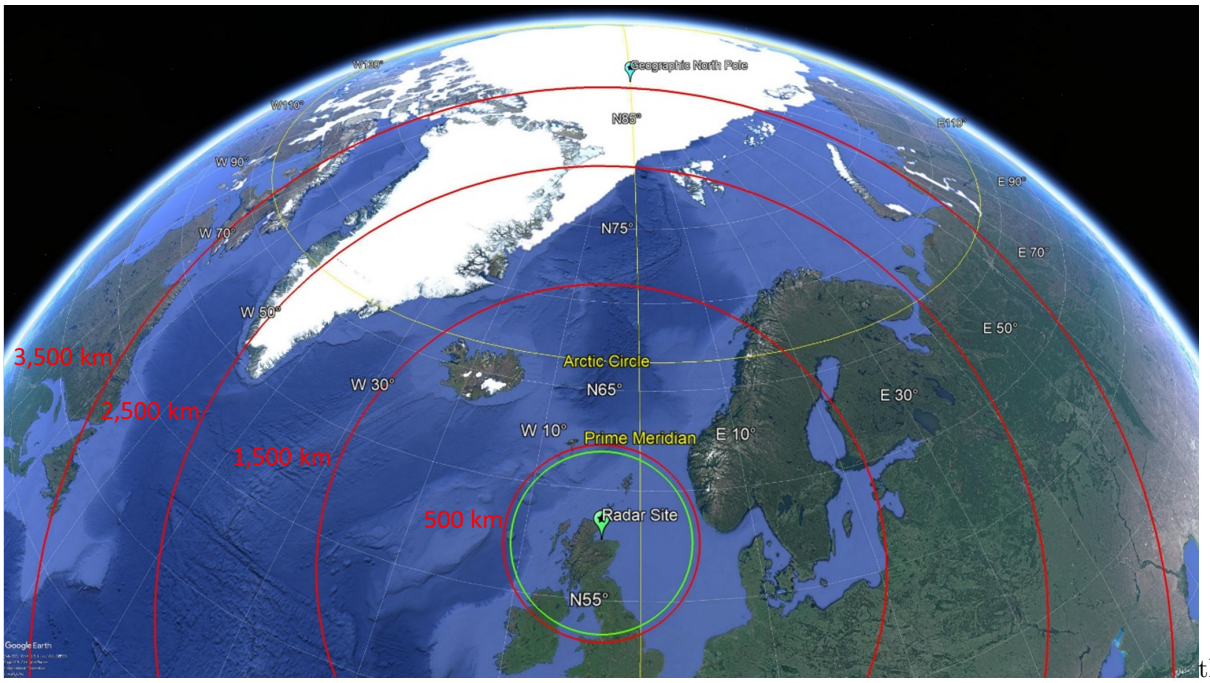


the clear advantage in coverage area offered by OTHR.

A frequency range of 5- to 26-MHz was designated to the OTHR, corresponding to the combination of a low and high band transmit array of 5- to 13- MHz and 13- to 26-MHz, respectively. A low band was included to evaluate the need for deploying the additional, larger, and more expensive low frequency array (Cervera, Francis, & Frazer, 2018). Propagation was limited to a single hop. The elevation range for the array was set to be 1-60° to enable propagation via different ionospheric regions for the given frequency range and conditions. Analysis of the radar was performed at a UTC time of 00:00 to coincide roughly with local midnight.

## Ionospheric Model

The electron density of the ionosphere experiences significant temporal and spatial variations with solar cycle, time of day, and season, necessitating the use of a suitable model that considers all these factors. At high latitudes, the scarcity of suitable data means the ionosphere is often poorly modelled within this region. The E-CHAIM ionospheric model, available at https://chain-new.chain-project.net, is used herein as it promises a more reliable interpretation of the high latitude ionosphere over the IRI (Themens et al., 2017, 2019a). The increased horizontal resolution and consideration of particle precipitation [Watson et al., 2021] make E-CHAIM far more suitable for representing the arctic ionosphere as the basis of the OTHR propagation study. E-CHAIM makes use of several sub models to form a holistic consideration of the ionosphere to ensure

the output electron density profile is reliable and covers a full range of altitudes and conditions (Themens et al., 2017, 2018, 2019b). Like the IRI, E-CHAIM takes NmF2 (F2 peak density) and hmF2 (F2 height) as the anchor point for the full electron density profile, with sub models used to represent the different regions. For this investigation, the Storm, Precipitation and D-region models are used with version 3.2 of E-CHAIM that has been modified to allow the user to input their own AE index for the auroral E-Region model. This allows one to modify the auroral conditions used without modifying the background ionospheric state so that an assessment of varying auroral conditions can be assessed independently. The individual and combined effects of these sub models on the density profile are illustrated in Figure 2 for within the auroral zone.

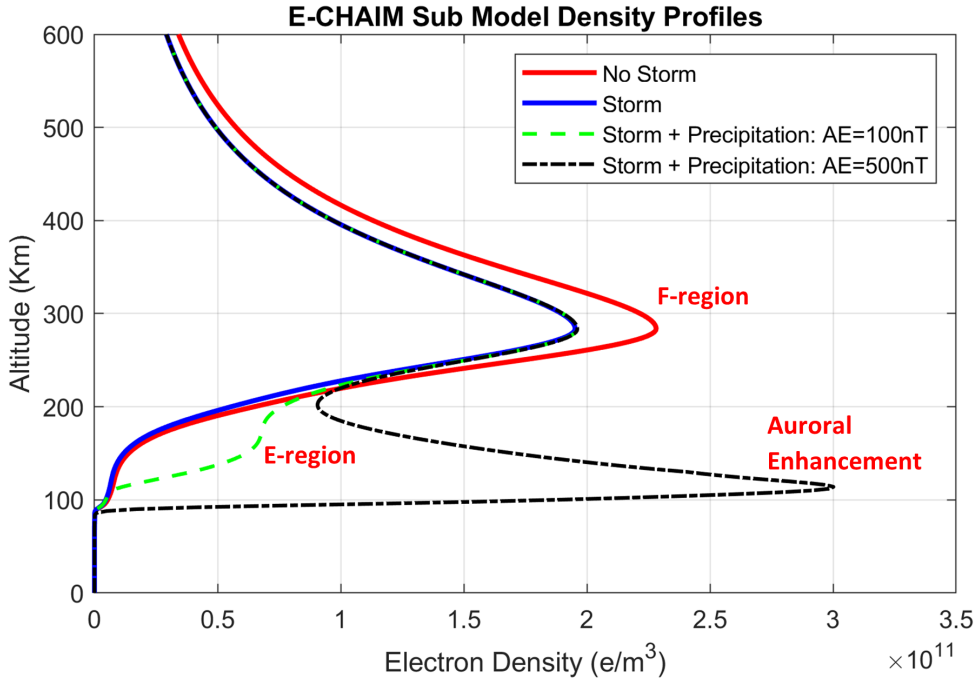


Figure . Vertical electron density profile at 65°N 0°W within the auroral zone showing the E-CHAIM sub-models for 15th July 2010 at 00 UT. A pronounced E-region enhancement introduced by an artificial aurora with an AE index of 500 nT is clear at an altitude of ~110 km. The D-region sub-model is active for each of the profiles but has no effect.

In the night sector, the D-region model option plays virtually no role due to the lack of ionisation; however, for rays that do propagate into the day sector, the inclusion ensures that this region is correctly modelled. The NmF2 Storm model option in E-CHAIM represents the decrease in NmF2 in response to thermospheric composition changes and enhanced recombination during geomagnetic storms (Themens et al., 2018). The effect of this model is seen in Figure 2 by

the clear reduction of the F-region peak density compared to the default model.

Alongside perturbations to NmF2, geomagnetic storms introduce enhanced levels of particle precipitation into the high latitude ionosphere, confined predominantly to the auroral zone. The precipitating particles collide with the dense neutral atmosphere and provide a source of ionisation. To accommodate the enhancement in E-Region electron density resulting from auroral particle precipitation, the E-CHAIM precipitation model option is included. The model covers the ionisation contribution from electrons with energies in the range of 1- to 30-Kev to form an enhanced density profile as described by Themens et al. (2020) and Watson et al. [2021]. In its current state, the range of energies considered by the precipitation model do not extend to sufficiently high energies to fully represent auroral absorption effects and so the focus of this study is directed to the analysis of propagation modes and MUF. E-CHAIM characterises auroral flux and energy of based on the hourly Auroral Electrojet (AE) index. With the modified form of E-CHAIM used herein, AE index can be input with a value in the range of 0- to 1300-nT. In doing so, the modification essentially permits the user to directly scale the auroral enhancement at will. This generates artificial aurora for a given UTC time so that a direct comparison of auroral effects can be made, isolating the climatological conditions of the ionosphere. In Figure 2, the E-region enhancement introduced by the precipitation model can clearly be seen.

It should be noted that the precipitation components of E-CHAIM are driven completely independently of the other components of the model, such that varying the AE used for the precipitation model will not change the background ionosphere upon which the precipitation is imposed. This is mainly due to the other components of the model relying not on the current geomagnetic state, like the precipitation model does, but rather on a time history of geomagnetic activity [Themens et al., 2017].

## HF Raytracing

This study will employ NRT to several scenarios, including system coverage tests in section 3.1, a propagation sensitivity analysis in section 3.2, a target intercept analysis in section 3.3, and an event case study in section 3.4. NRT is a widely employed technique used to study the propagation of HF radio waves through the ionosphere and is well suited to OTHR applications. This study uses the PHaRLAP HF ray tracing toolbox Version 4.4.2, including both 3D and 2D NRT solvers, with E-CHAIM acting as the ionospheric electron density model for the NRT. 3D NRT was implemented to investigate coverage and target interception, whilst for our propagation sensitivity, case study analysis, 2D NRT was used to reduce computation time (Cervera, Francis, & Frazer, 2018). The latest version of the PHaRLAP code can be accessed at https://www.dst.defence.gov.au/opportunity/pharlap-provision-high-frequency-raytracing-laboratory-propagation-studies. Linear interpolation of the 2D and 3D ray position data was performed to slice the data at a specified target

altitude of 10 km, under the condition that the ray is not rising to avoid rays leaving the source.

## Ionospheric Conditions

To assess the effect of aurora on the propagation of HF radio waves transmitted from the hypothetical OTHR system, we have identified six periods to use as case studies, for which we will first examine the coverage area and frequency availability behaviour of the hypothetical radar before comparing target tracking capacity with and without aurora for a pair of flight paths through the OTHR's field of view. Variations in auroral effects are evaluated based on solar cycle, season, and auroral intensity using the tools and methods outlined in the previous three subsections. Two solar activity levels from solar cycle 24 were selected for the cases, with high solar activity cases taken from 2013 and low solar activity cases taken from 2010. The baseline conditions presented in Table 1 were investigated at midnight for two artificial ionospheric states: aurora induced with AE equal to 500 nT and precipitation removed with AE equal to 0 nT. Table 1 outlines the F10.7 flux, the 81-day smoothed F10.7 flux, the AE index, the integrated AE index (AE_I), and the Kp index for the selected periods. Integrated AE index, a time weighted geomagnetic index based on the method outlined in Wu & Wilkinson (1995), is included here as it is used as a primary driver in the storm NmF2 and thickness models within E-CHAIM; as such, AE_I is indicative of the actual conditions represented by the non-precipitation E-CHAIM components. Similarly, as E-CHAIM uses 81-day smoothed F10.7 flux to drive its solar activity behaviour, F10.7_81 is also more indicative of the modelled conditions than F10.7 flux itself. The selected dates in Table 1 were chosen under the requirement that the geomagnetic and solar conditions (F10.7_81 and AE_I) are consistent between the cases; this is important to avoid conflating these effects with expected seasonal and solar activity variations when making comparisons.

*Table 1. Details of The Ionospheric Cases Investigated at UTC 00:00. AE index, integrated AE index and 81-day integrated F10.7 flux (AE_I) were taken from the E-CHAIM database*

| **Case ID** | 1 | 2 | 3 | 4 | 5 | 6 |
|---|---|---|---|---|---|---|
| **Date** | 10/01/2010 | 19/04/2010 | 13/06/2010 | 04/01/2013 | 09/04/2013 | 16/06 |
| **Month** | January | April | June | January | April | June |
| **Year** | 2010 | 2010 | 2010 | 2013 | 2013 | 2013 |
| **Solar Cycle** | Min | Min | Min | Max | Max | Max |
| **F10.7 Flux (sfu)** | 84 | 75 | 76 | 142 | 147 | 116 |
| **F10.7 Flux 81-day (sfu)** | 78.14 | 78.33 | 76.57 | 112.1 | 123.5 | 121.3 |
| **AE Index (nT)** | 10 | 42 | 48 | 15 | 50 | 70 |
| **Integrated AE Index (nT)** | 19.44 | 39.76 | 51.88 | 28.56 | 57.9 | 96.26 |
| **Kp index (GFZ Potsdam)** | 0 | 1+ | 1- | 2- | 1+ | 0+ |

Despite AE index driving the precipitation sub model, it is not essential that AE values are equal between the cases due to the use of the modified version of E-CHAIM allowing the AE parameterisation index to be overridden with selected AE values. In the case of this paper, AE values of only 0- and 500-nT were used to artificially toggle aurora. It is well known that seasonal variations in solar activity and the solar cycle have a profound effect on the electron density with large modifications seen yearly and seasonally. For this reason, it was necessitated that solar activity be uniform for the cases within each 2010 and 2013.

For each of the aforementioned cases, E-CHAIM was used to generate ionospheric grids covering the arctic region down to a latitude of 55°. An altitude range of 60- to 382-km was covered at a resolution of 2 km to model the ionosphere between the D-region and F2 peak. Latitude was incremented by 0.5° whilst longitude by 1°. A total of 12 cases were investigated for coverage and target interception.

# Results

To demonstrate the structure of the modelled aurora, the electron density at 102.5 km altitude, with and without the auroral E-Region model turned on, is presented in Figure 3 for both low (A) and high (B) solar activity conditions and all case periods. This altitude is chosen for this demonstration to coincide with the 102.5 km altitude of the quiet E-CHAIM model's E-Region peak.

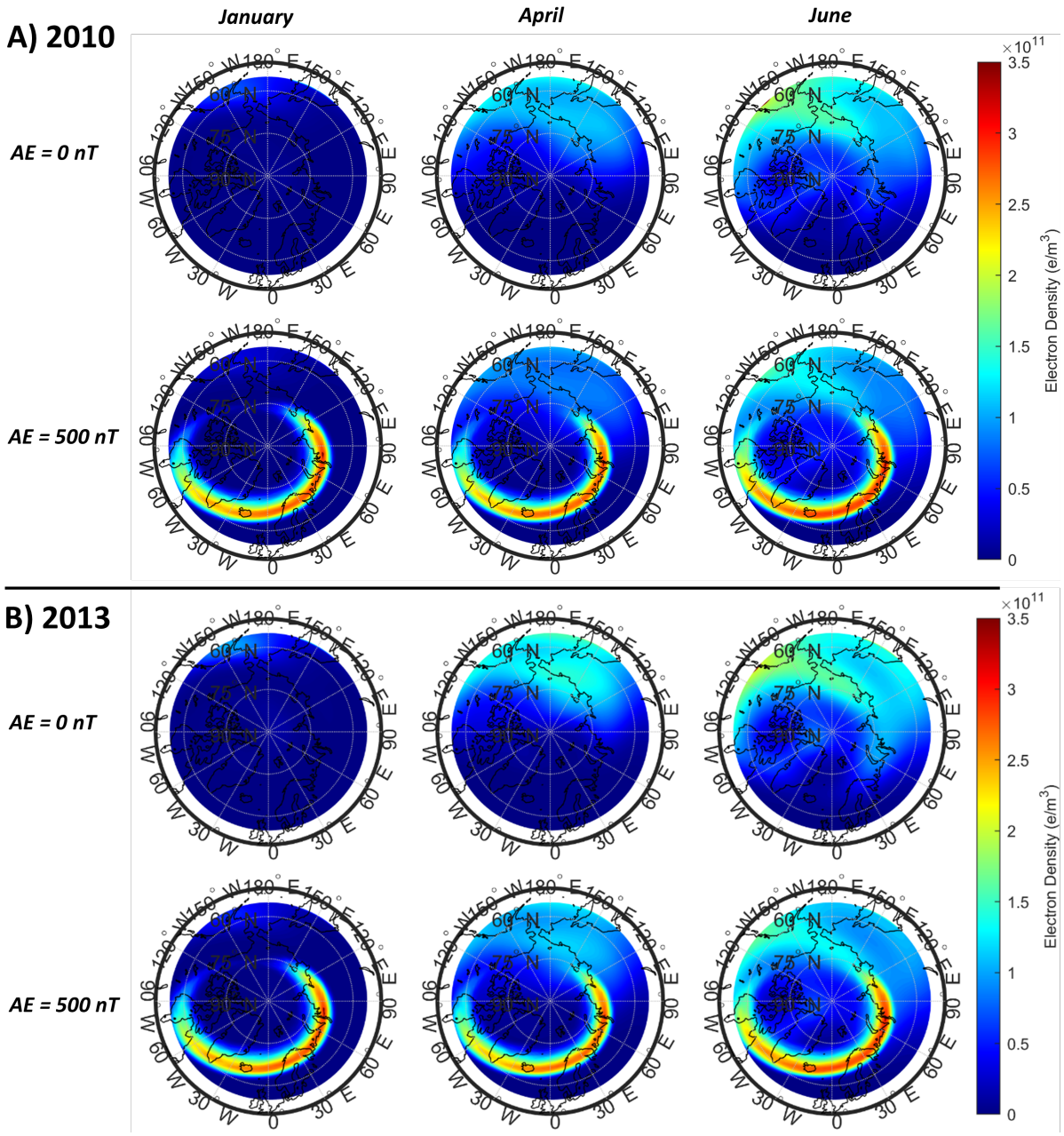


Figure . Electron density distribution at 102.5km altitude for A) low solar activity (2010) and B) high solar activity (2013) showing dayside and auroral enhancements to the E-region. Note the clear auroral oval for cases with precipitation. The D-region, Storm and Precipitation models were active in each plot.

Aurora were seen in cases with precipitation active, indicated by an enhancement of E-Region electron density in an oval band centred on the geomagnetic north pole. Maximum auroral ionisation occurred at longitudes between 0.00°E and 30°E, relating to a local time between 00:00-02:00. For an AE index of 0 nT (precipitation off), the background conditions without enhancement are shown. With precipitation off, there remains little to no electron density in the auroral oval and polar cap regions at E-Region altitudes, due to a lack of photoionization. During summer and equinox periods background E-Region densities on the dayside are enhanced, but nightside conditions remain largely depressed. In this way, aurora induced by the model at an AE of 500 nT dominates the nightside electron density distribution in general. Further increasing AE index is expected to simply induce a more intense auroral oval marked by an equatorward shifting of the oval band, an enhancement in peak NmE, and a broadening of the oval band.

## System Coverage

To examine the coverage of the hypothetical OTHR system, we employ PHaRLAP simulations through the E-CHAIM ionosphere with and without auroral enhancements to the E-Region. In this study, the PHaRLAP 3D engine was used to generate fans of rays, where elevation angle is incremented by 1°, frequency is incremented by 0.5 MHz, and azimuth is incremented by 0.9375°, for a total of 495,360 rays. These raytracings are conducted for each of the six cases, with AE index for the auroral model set to 0 nT and 500 nT for each case. The ionospheric grids illustrated in the previous section were used for the propagation medium.

The available frequency coverage for a target altitude of 10km is presented in Figure 4, showing large variations in coverage area for the model radar with both climatological and auroral conditions. Figure 4 shows the maximum frequency coverage as the greatest frequency rays are plot on top of lower frequency points. Rays corresponding to both O- and X-modes are plotted here together. Based on these echo distributions, maximum frequency and median range for each case was determined by taking the overall median of the full set of ray ground ranges and by selecting the greatest frequency supported for each case, respectively. The percentage of useable rays is the proportion of rays passing through the reference altitude and indicates the total number of non-penetrating rays that provide actual OTHR coverage. Table 2 presents this selection of data values for each of the cases.

Table . Data values extracted from the hypothetical OTHR coverage raytracing test.

| **Case ID** | **Date** | **AE Index (nT)** | **% Rays Useable** | **MUF (MHz)** | **Median Range (km)** |
|---|---|---|---|---|---|
| 1 | 10/01/2010 | 0 | 1.26 | 8.5 | 2542 |
| 2 | 19/04/2010 | 0 | 4.91 | 11.5 | 2128 |

| Case ID | Date | AE Index (nT) | % Rays Useable | MUF (MHz) | Median Range (km) |
|---|---|---|---|---|---|
| 3 | 13/06/2010 | 0 | 12.23 | 14 | 1728 |
| 4 | 04/01/2013 | 0 | 3.09 | 12 | 2394 |
| 5 | 09/04/2013 | 0 | 12.38 | 14.5 | 1997 |
| 6 | 16/06/2013 | 0 | 26.65 | 18 | 1468 |
| 7 | 10/01/2010 | 500 | 9.47 | 26 | 1226 |
| 8 | 19/04/2010 | 500 | 9.07 | 26 | 1227 |
| 9 | 13/06/2010 | 500 | 11.93 | 25 | 1323 |
| 10 | 04/01/2013 | 500 | 9.14 | 26 | 1243 |
| 11 | 09/04/2013 | 500 | 12.55 | 26 | 1420 |
| 12 | 16/06/2013 | 500 | 25.91 | 25 | 1357 |

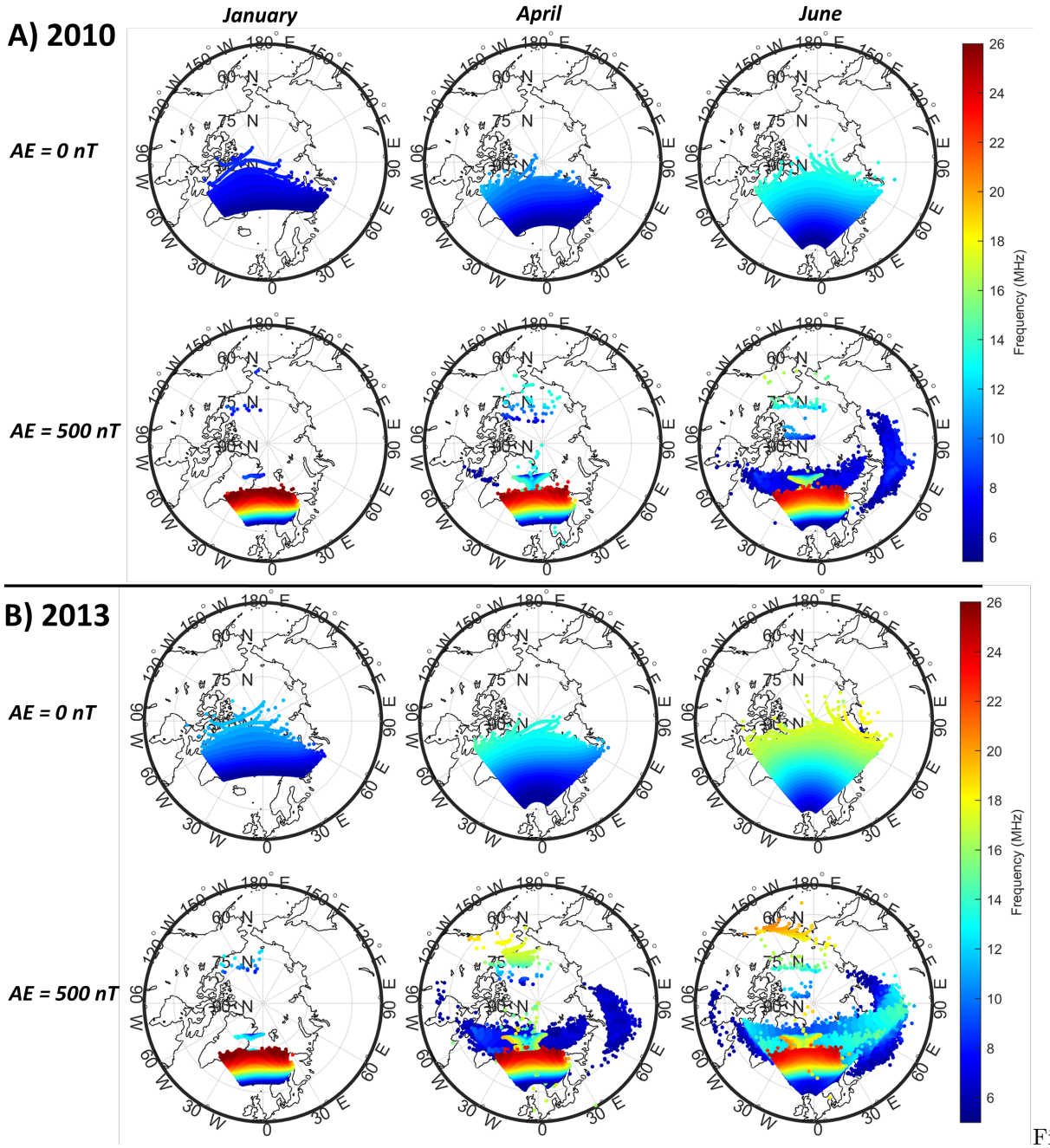


Figure 4. Frequency coverage for A) low solar activity (2010) and B) high solar activity (2013) for each case outlined in Table 1 at a target altitude of 10 km for both precipitation OFF, and aurora induced with AE index set to 500 nT. The E-CHAIM storm and D-region models were active for all subplots.

Coverage area is seen to be greatest without precipitation, with rays intercepting the full 90° sector for a large selection of ranges. Overall median range for cases without aurora was between 1468- and 2542-km whereas with precipitation, the median was between 1226- and 1420-km. The lack of precipitation produced ideal ionospheric conditions with only a cohesive F-region remaining. Because of this, the ionosphere acted as an ideal spherical shell reflector as shown in Figure 5A, producing the even coverage observed in Figure 4. Furthermore, without precipitation, low frequency rays dominated the coverage area; the maximum frequency supported by the F-region reached only 18 MHz for June 2013 whereas for induced aurora, it was consistently above 25 MHz. To further examine the nature of the propagation conditions summarized in Figure 4, propagation cross sections are plotted in Figure 5 using 2D NRT for a subset of conditions and present three distinct propagation modes.

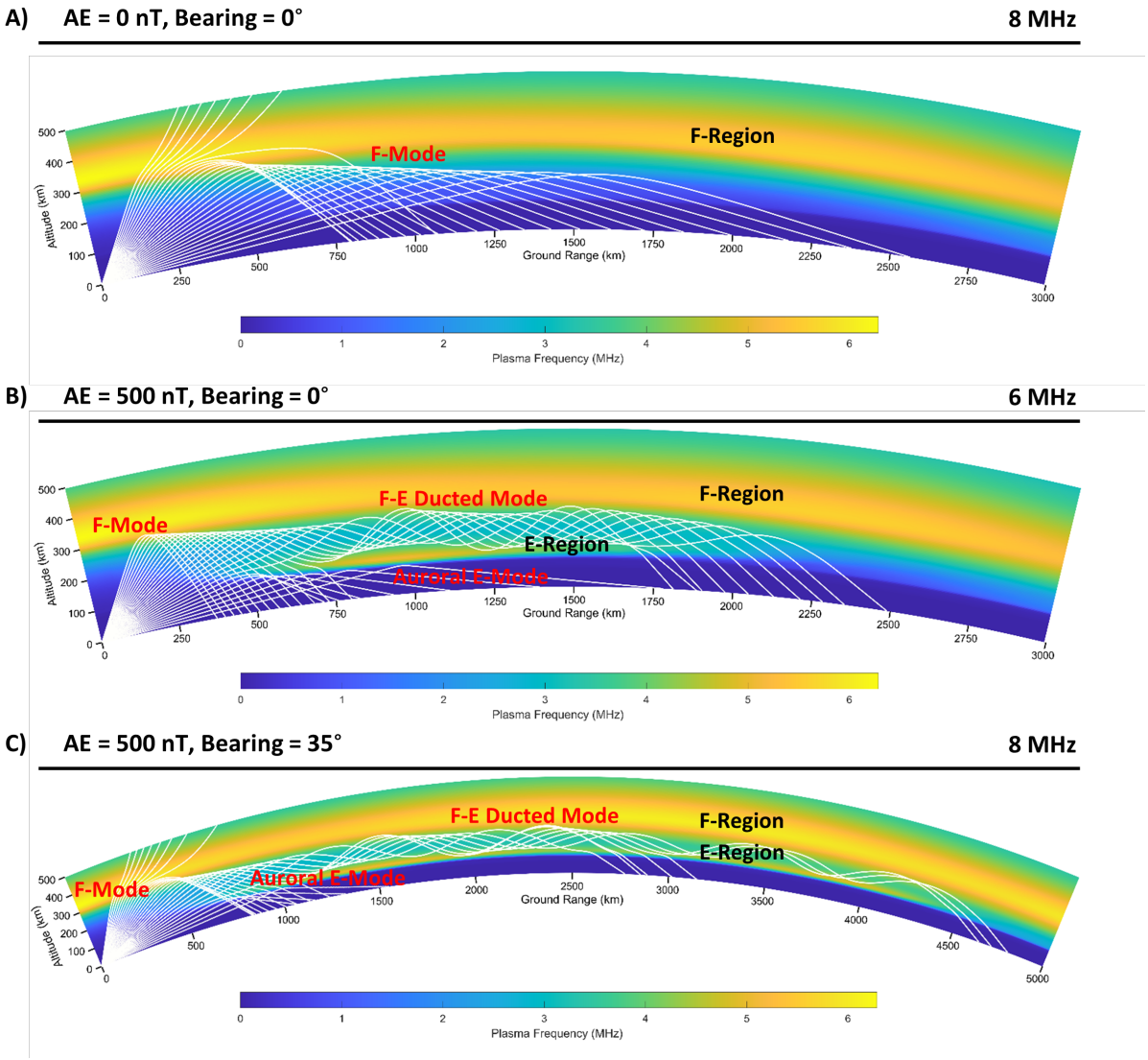


Figure 5. 2D NRT propagation cross section plots for the model OTHR under different conditions and frequencies on the 16th of June 2013 showing in: A) the F-region of the ionosphere acting as an ideal reflector with no precipitation active; B) the three propagation modes present with aurora providing different bands of ranges; C) long range ducted propagation along the auroral oval at a bearing of 35° from boresight. The Storm and D-region sub models of E-CHAIM are active in each.

With precipitation, three distinct propagation modes were active in the presence of auroral enhancements as illustrated in Figure 5B: F-mode, Auroral E-mode and F-E ducted mode. The sharp drops in frequency observed with aurora signi-

fied distinct changes in propagation mode. This was most notably seen in Figure 4 for April and June both years as a patch of high frequency Auroral E-mode rays overlaid onto low frequency F-E ducted rays. Auroral E-mode propagation produced small sectors of high frequency coverage at latitudes between 60°N and 75°N wherein the greatest frequency support was available. A consequence of this was that the auroral enhancement blocked rays that would otherwise propagate via F-mode and reach greater ranges. This was clear in April 2010 and January of both years with artificial aurora as coverage was reduced to a small sector of Auroral E-mode rays. For these cases, overall median range did not exceed 1243 km. Despite the reduction in coverage area and available range, aurora provided a noticeable increase in MUF, with a maximum improvement of 17.5 MHz from 8.5MHz to 26MHz in January 2010.

In most cases, the F-region was still accessed by some low frequency rays, providing bands of coverage centred at approximately 80°N and at extremely close ranges. For the band at 80°N, propagation did not occur directly via the F-region and instead, the descending rays were ducted by aurora between the F- and E-regions; this is the basis of F-E ducted mode. Auroral ducting introduced large side lobes with coverage over northern Russia, and in some limited cases, the Canadian arctic. This occurred as low frequency rays were ducted for great distances along the auroral oval. Figure 5C illustrated this mechanism for over Russia in June 2013, with numerous hops occurring. The lobe shape formed as rays were unable to return to the surface for several thousand kilometres once above the auroral oval. In the aforementioned cases, it can be seen that the rays land at a bearing exceeding the azimuthal field of view (FOV) of the radar, implying lateral reflections. Ducted, low frequency rays therefore dominated long-range coverage for cases with both aurora and strong F-regions. For solar minimum, overall coverage was reduced in comparison to the equivalent conditions at solar maximum in most cases. This was due to the stronger F-region enabling low frequency propagation.

## Propagation Sensitivity to Auroral Intensity

To further examine the change in propagation conditions with increasing auroral intensity, we here perform 2D-NRT from our hypothetical OTHR system at boresight with AE indices ranging from 0- to 1300-nT, incremented by 6.5 nT. Rays were propagated with a frequency and elevation increment of 0.5 MHz and 0.75°, respectively. In total, 679,400 rays were generated for each case. Range was plotted against AE with a colourmap representing frequency in Figure 6 for each climatological condition outlined in Table 1.

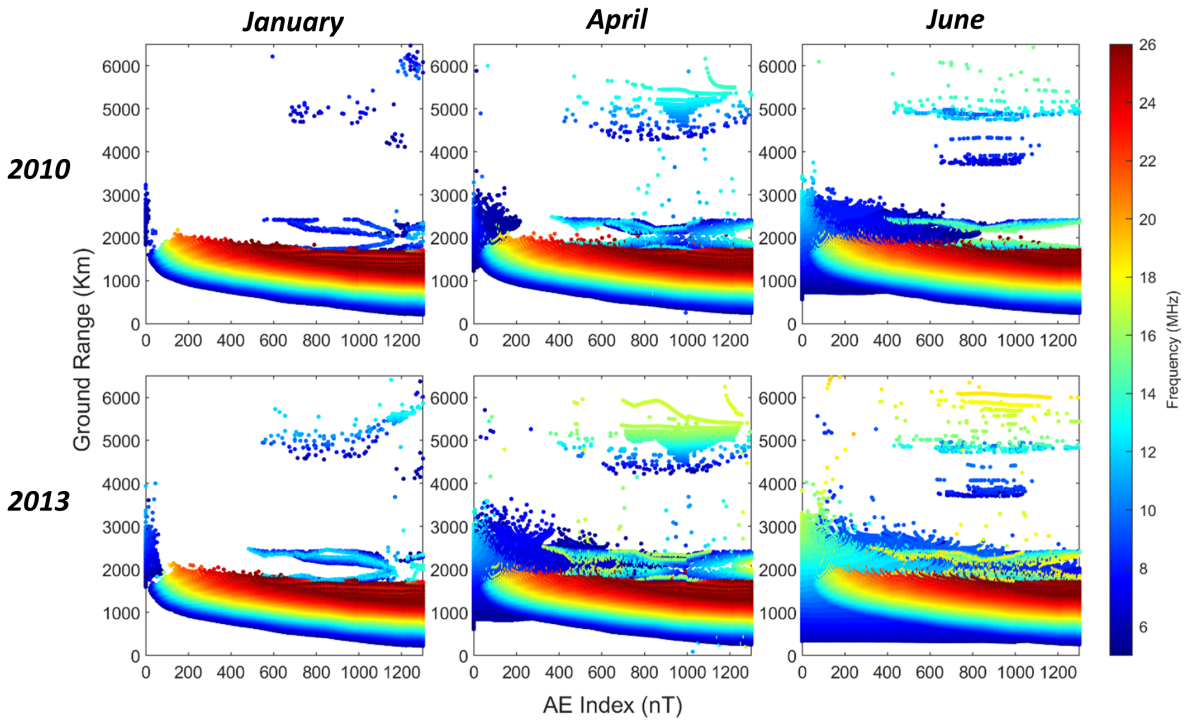


Figure 6. Propagation sensitivity presented by range versus AE index with a frequency colourmap for 6 climatological conditions. Note the transition at 50 nT.

These figures showed that without auroral enhancements only low frequency, high elevation, F-mode propagation is supported. For AE index between 50- and 200-nT, a transition region was seen for all cases, marking the addition of Auroral E-mode and F-E ducted propagation. During this transition, F-mode propagation providing ranges between 1,000- and 3,000-km becomes partially blocked by the developing E-region. This occurred once the E-region was sufficiently established at an AE index of around 50 nT. Increasing auroral intensity was shown to reduce range for all cases by around 1000 km at high AE index. A significant loss in coverage was not seen for April 2013 nor in June both years, as low frequency support remained for F-E ducted rays. For April 2010 and both December cases, ducted propagation did not occur due to the weakly ionised F-region; this resulted in support for only the E-mode. Bands of long-distance rays between 4,000- 6,000 km were observed above 500 nT, with this propagation demonstrated in Figure 7 using 2D-NRT. The enhanced range occurred for a small proportion of rays that missed the reference altitude after being reflected by aurora, before

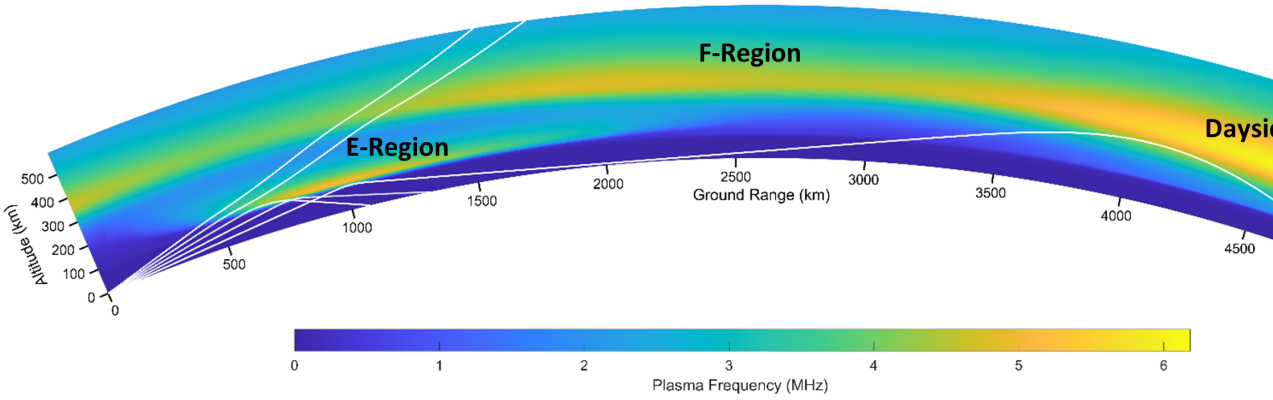


reflected to the surface by the dayside ionisation.

Figure 7. 2D NRT cross section for the model OTHR at boresight for April 2013 with AE set to 500 nT, showing long range propagation of rays skimming the reference altitude.

## Target Intercept Analysis

To assess the hypothetical OTHR's capacity to intercept a target under different ionospheric conditions, two commercial flightpaths are tasked for monitoring by the radar, as detailed in Table 3 and illustrated in Figure 8. The flightpath is described as a great circle path between the two endpoint coordinates. The azimuthal extent of the radar field of view (FOV) only covers 75- and 67-% of flightpaths A and B, respectively. This is marked in Figure 8 by the outer dashed red lines. Accounting for the FOV restriction, actual path coverage was determined using Equation 4**.**

$$\%\text{Coverage}_{\text{actual}} = \frac{\%\ path\ intercepted}{\%\ FOV} \#4$$

Rays passing through the target altitude within 15 km of the path were deemed as a successful intercept, with the maximum frequency ray selected from each point on the path as the optimal frequency; in practice, higher frequency rays offer practical advantages for OTHR.

Table 3. Specific Details of the Selected Commercial Flight Paths, Including Path Length.

| Flight Path | Start Location | End location | Start Coordinates | End Coordinates | P |
|---|---|---|---|---|---|
| A | Oslo, Norway | Longyearbyen, Svalbard | 60.15N, 11.10E | 78.22N, 15.62E | 2, |
| B | Helsinki, Finland | Reykjavik, Iceland | 60.19N, 24.57E | 64.70N, 21.56W | 2, |

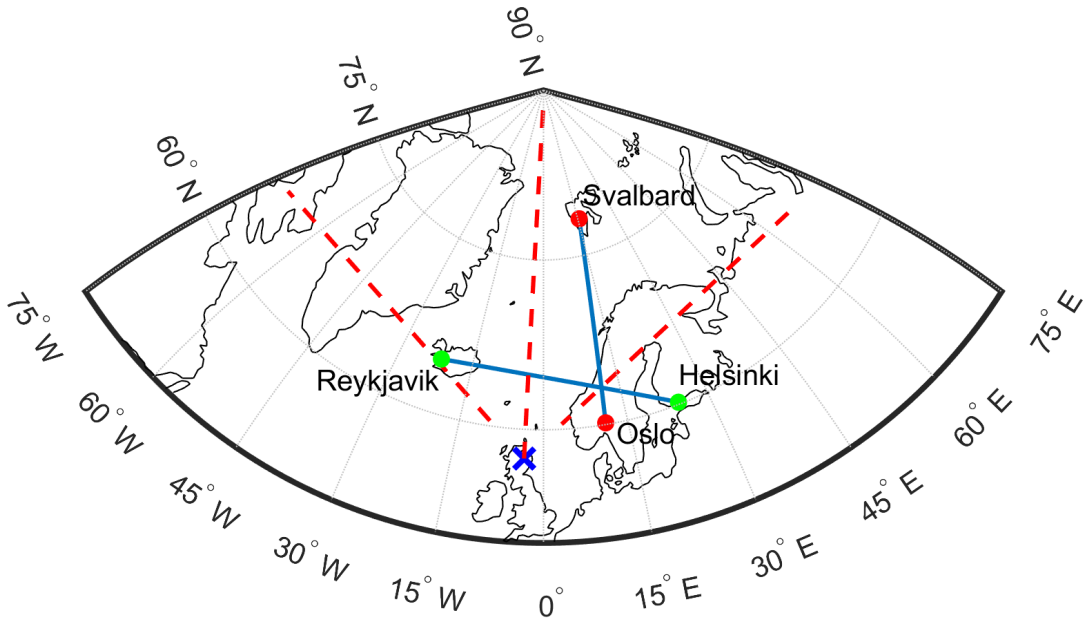


Figure 8. Map showing flightpaths A and B in red and green, respectively. The radar location is marked by a blue cross with boresight and azimuthal field of view shown with red dashed lines.

Maximum frequency rays intercepting the flight paths were plotted for all 12 cases against normalised distance using data from section 3.2 and is presented in Figure 9.

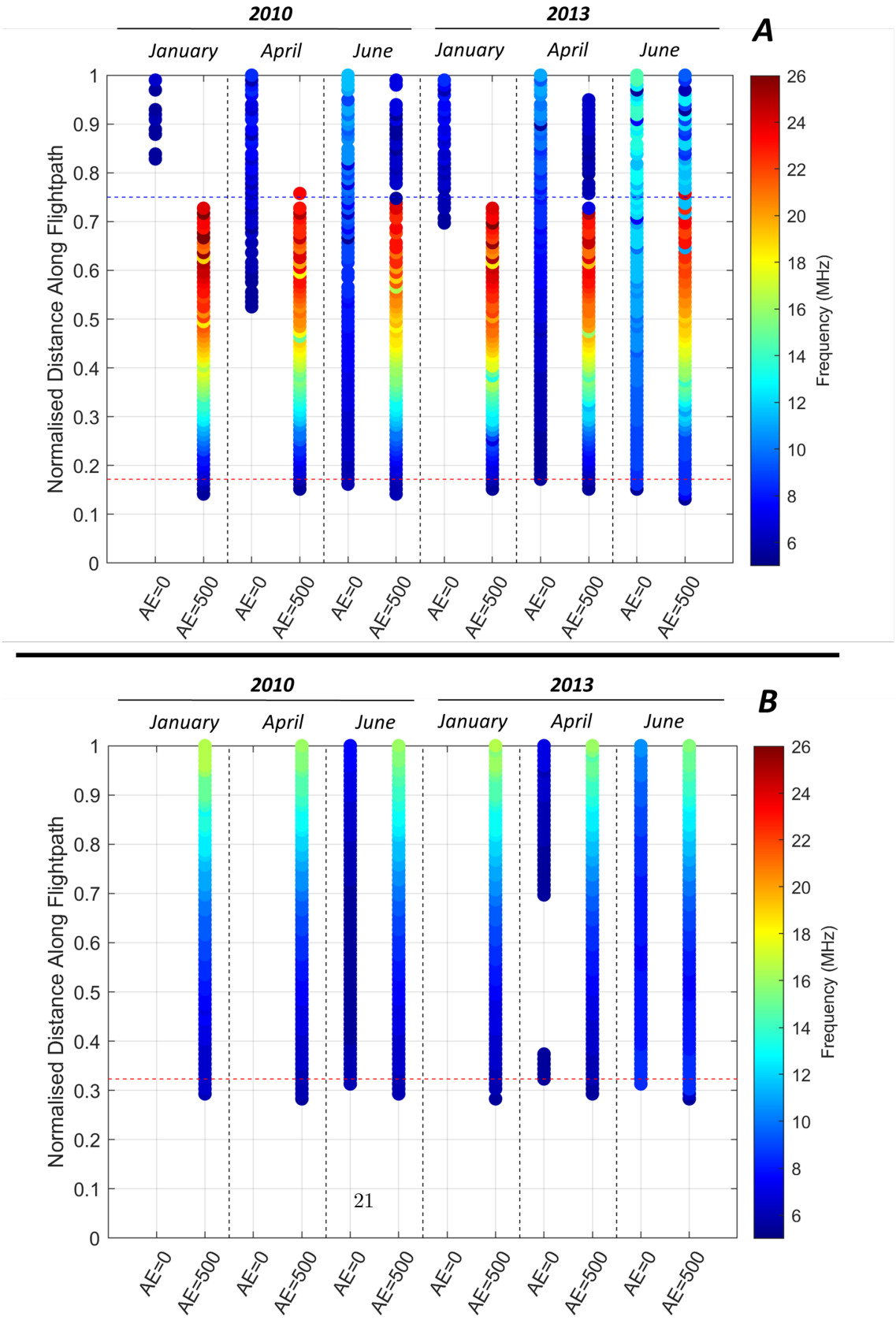
A
2010
2013
January
April
June
January
April
June
Normalised Distance Along Flightpath
Frequency (MHz)
AE=0
AE=500
B



Figure

9. Frequency coverage for flightpath A and B, showing an increase in MUF and range with artificial aurora. In both subplots A and B, the azimuthal extent of the OTHR field of view is marked by a red dashed line, making clear that nominal coverage exceeds 100% in some cases. In subplot A, the mode transition from Auroral E-mode to E-F ducted propagation is signified by the drop in frequency at a distance approximately 75% along the path and is highlighted by a blue dashed line. For subplot B, no target coverage is seen for three cases without precipitation. Note that the E-CHAIM storm and D-region models were active for all flightpath analysis.

In Figure 9, the presence of aurora was seen to increase MUF for a considerable portion of both flightpaths A and B; MUF reached 26 MHz in some cases of flightpath A with artificial aurora, compared to the maximum of 14.5 MHz without precipitation. The proportion of both paths covered was lowest during January and April without aurora, falling to a minimum of 12% for flightpath A. In the case of flightpath B without aurora however, no frequencies were available to cover any proportion of the path during times of low solar activity, including January both years and April 2010. This is likely due to the weak F-region not supporting the high elevation rays required to achieve extremely close in coverage, the region in which flightpath B intercepts. This is further supported by the lack of echoes at ranges close to the radar in Figure 4B during these periods. Maximum coverage reached 115% for June 2013 with aurora, where additional coverage over 100% was achieved due to lateral deflection of rays toward the east that occur due to the presence of aurora. Overall, the percentage of path intercepted was matched or else improved with the inclusion of aurora as indicated in Figure 9, contrary to the reduction in coverage area noted in Figure 4. This makes clear that auroral propagation can provide acceptable coverage when a strong F-region is available, providing that close range detection is required. Of course, absorption and auroral clutter may render such improvements in coverage non-viable and further work with accommodation for auroral absorption will be necessary to assess this limitation.

## Case Study: May 2010 Geomagnetic Storm

To further examine the evolution of OTHR system coverage during geomagnetic disturbances, we here conduct further comparisons of propagation conditions during a case study geomagnetic storm event. A relatively long but moderate geomagnetic storm between the 21$^{st}$ May and 7$^{th}$ June 2010, with a peak on the 29$^{th}$ of May, is selected as a case study to investigate the effects of disturbed space weather on the model OTHR over time. This event was chosen as E-CHAIM has previously been validated in Themens et al. (2017) for this period, showing improvements of between 30-35% in some regions over the IRI and tracking the negative ionospheric response to the storm very well in the polar cap. The variation in available target range and MUF with time will be investigated during the event using 2D-NRT at boresight.

The variation in ground range and maximum frequency at boresight was plot-

ted through the duration of the 2010 May geomagnetic storm between the 21$^{st}$ May and 7$^{th}$ June 2010. Time resolution was limited to hourly intervals due to E-CHAIM's parametrisation using hourly indices for driving the ionospheric models. The case study was investigated for three E-CHAIM setups: Precipitation and Storm active; Storm active with Precipitation inactive; Precipitation and Storm inactive. A frequency and elevation resolution of 0.5 MHz and 0.75°, respectively was used for a total of 1,222,920 rays in each setup for the 360 individual hourly steps. Figure 10 presents the case study data with inclusion of AE index data taken from the World Data Centre for Geomagnetism Kyoto, available at: http://wdc.kugi.kyoto-u.ac.jp/aedir/.

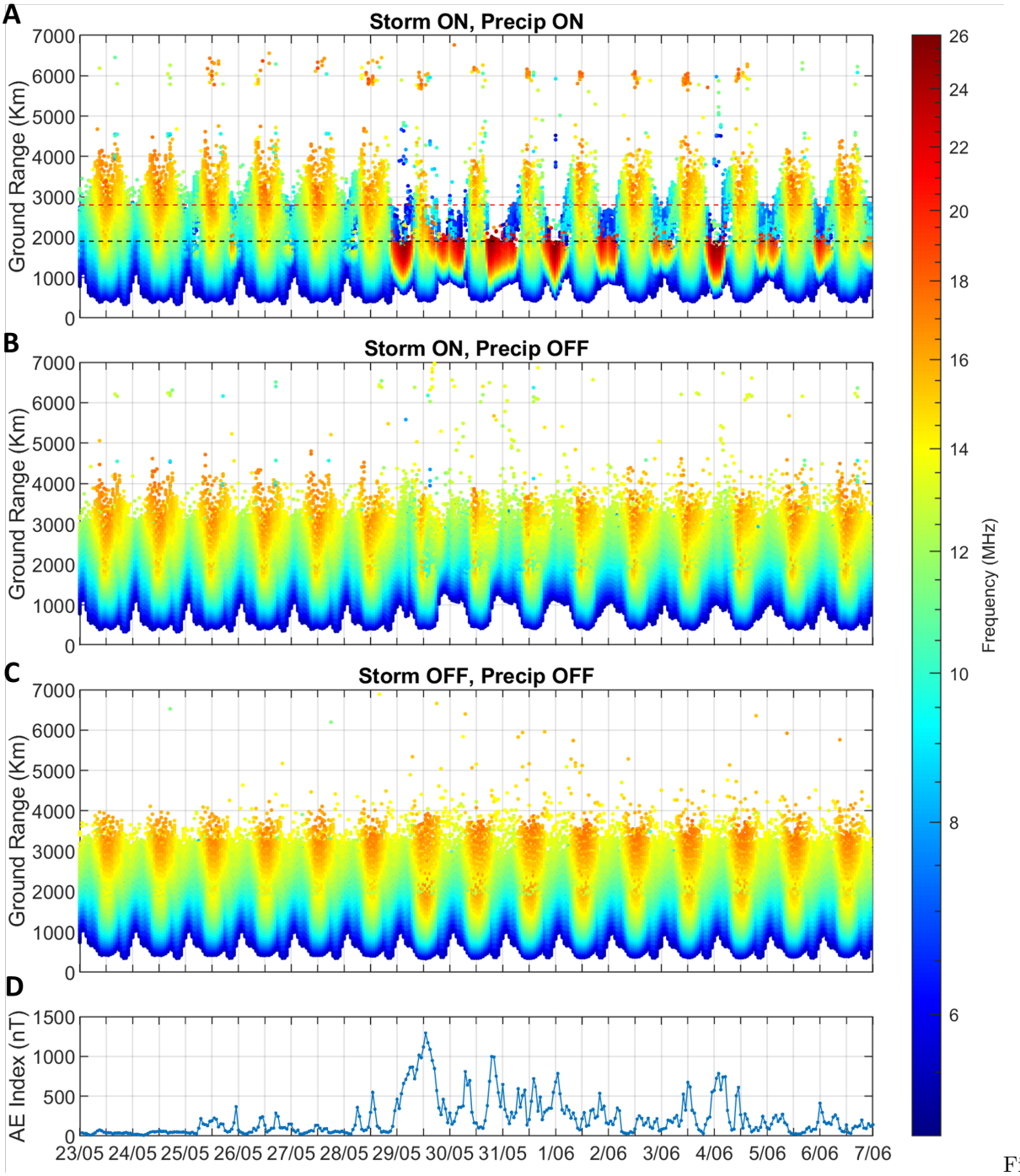


Figure 10. Variation in frequency and ground range with time during the peak of the

2010 May geomagnetic storm with different combinations of the E-CHAIM precipitation and storm sub models active. The 2D NRT is performed for the hypothetical OTHR at boresight. Note that a log scale is used to represent frequency in the colormap. Subplot A represents the optimal setup of E-CHAIM for auroral conditions due to consideration of both precipitation and storm effects. The inclusion of subplot B directly shows the resulting propagation environment with auroral ionisation removed, effectively making clear the effect of precipitation when compared to A. Quiet conditions are represented in subplot C by the removal of both ionospheric effects. AE index data is included for comprehension of geomagnetic conditions in subplot D. Red and black dashed lines in subplot A indicate the nominal maximum nighttime range prior to and during the storm with induced precipitation, respectively.

With both sub models inactive, the isolated effects to both range and frequency induced by diurnal variations in photoionization and ion recombination are modelled, representing a basic, undisturbed ionosphere. This is shown in Figure 10 Subplot D by the repeating pattern of range and frequency. Despite storm and precipitation effects being inactive in E-CHAIM for this case, differences in frequency between the days are still observed at a range of ~2,000 at the onset of the storm on the 29$^{\text{th}}$ of May and this is in contrast to what is expected during quiet periods. This is due to geomagnetic driving in other components of the E-CHAIM model, namely in the E-CHAIM bottomside thickness. During the storm, the bottomside in E-CHAIM broadens slightly, causing the observed differences. An interested reader may consult Themens et al. (2019b) for a detailed overview of the bottomside thickness model.

With precipitation active, a clear addition of high frequency close range coverage, provided by auroral ionisation, is observed at nighttime throughout the duration of the storm, most notably from the 29$^{\text{th}}$ of May onwards. This addition is representative of auroral E-mode propagation support and is marked by a sharp drop in nominal nighttime range from ~2,800 km down to ~1,900 km and a significant increase in MUF from approximately 12.5 MHz to 26 MHz. The change in coverage due to this introduction of auroral precipitation is marked in subplot A by the red and black dashed lines. With aurora present during and after the peak of the storm, auroral F-E ducted propagation is also identifiable by the patches of low frequency rays between 2,000- and 3,000-km during the night. There is a sudden transition from high frequency Auroral E-mode and low frequency ducted F-E mode as the rays change from reflecting via the E-region instead to the F-region. This propagation acts to extend auroral propagation out to 3,000 km in some cases, as seen in subsections 3.1 and 3.2. The MUF and duration of the auroral coverage is at a maximum during the peak of the event, marked by the high AE index values reaching up to 1,293 nT on the 29$^{\text{th}}$ of May and is seen to extend into the daytime. A second, smaller peak with a magnitude of 786 nT, is also clear on the 4$^{\text{th}}$ of June, with a corresponding increase in Auroral E-mode propagation due to the presence of more intense aurora. It is also interesting to note that auroral propagation occurs even before the storm, as suggested by the small patches of higher frequency coverage rays at ~2,000

km between the 25$^{th}$ and 29$^{th}$ of May. The magnitude of such coverage is very subdued in comparison to the peak of the storm due to the lower geomagnetic activity shown in Figure 10C.

At the start of the time span in Figure 10A, the nominal maximum daytime range reaches out to approximately 3,200 km; however, through the peak of the geomagnetic storm, range falls short of this value with some days showing reductions of up to 600 km. This is evident of the NmF2 storm perturbation response modelled by the E-CHAIM storm sub model. When comparing Figures 10B and 10C, the effect of just the NmF2 response of ionospheric storm on the radar is isolated and clear, with MUF seen to noticeably decrease through the peak of the storm along with a minor increase in minimum range due of decreasing NmF2 during the storm. A small reduction in maximum range can also be observed. With this comparison, the storm recovery of the ionosphere can be noted by the general increase in MUF coverage back to pre-storm levels as the intensity of the storm reduces from the 29$^{th}$ May onwards to the end of the time range. Despite the Storm NmF2 model being active in both subplots A and B, daytime coverage is not seen to be identical between the two; this is due to auroral propagation lasting for more than 12 hours into the daytime in some cases as auroral ionisation remains. This reduces daytime range due to aurora blocking much of the direct F-mode propagation.

# Discussion

Aurora of varying strength are often present within the night side ionosphere due to ever present auroral particle precipitation, implying that aurora will often play a major role in the propagation of HF signals at high latitudes, where only the quietest conditions, characterized by AE index below approximately 50 nT, escape a significant alteration to MUF or propagation. This is seen prior to the transition regions noted in Figure 6. With the presence of auroral enhancements, foF2 significantly increases and permits the greater MUF values observed. This notable increase is due to the E-region auroral enhancement having a much greater peak level of ionisation in comparison to the weak nighttime F-region.

The high sensitivity to AE variations indicated that even mild aurora can substantially change the propagation environment. This suggested that an FMS capable of considering and adapting to aurora is paramount to practical OTHR deployments propagating through the auroral oval. In some cases, target interception may not be possible due to no available frequencies providing coverage to the region of interest due to variations in geomagnetic activity modifying the ionosphere. The presence of aurora was not detrimental in the target interception cases explored as coverage of flightpath B was consistent whereas this was not seen for three cases without auroral propagation. This was enabled by the addition of very short-range coverage provided by high elevation Auroral E-mode rays. The distinct propagation modes were observed to have significantly different path lengths in Figure 5, of which it is expected to cause delayed

soundings and noticeable path loss variations despite intercepting near regions. This further complicates FMS design as the system would need to distinguish between modes to accurately position targets. As explained by Riddolls (2006), OTHR are tasked to dwell on specific cells within the coverage area to observe targets, and this was expected to be convoluted by the regions of large frequency gradients caused by aurora.

A notable limitation of using the E-CHAIM climatological ionospheric model to simulate OTHR propagation, however, is that the relatively low spatial and temporal resolution is unable to capture the small scale auroral irregularities and horizontal gradients seen within the real electron density profile. Despite this, E-CHAIM offers the best potential for investigating aurora due to its increased resolution over the more commonly used IRI and capacity to provide at least statistical representation of auroral enhancements with greater fidelity. Without a greater density network of ionospheric sounders or satellite-borne auroral imagers, climatological modelling is currently the only option for a large-scale representation of the ionosphere. The aforementioned auroral irregularities can reflect radio waves propagating through the auroral zone horizontally and have been observed to cause azimuthal deviations from great circle paths of up to 90°-100° (Bates, Albee, & Hunsucker, 1966; Hunsucker & Bates, 1969; Rogers, Warrington, & Jones, 2003). This was noticeable in Figure 4B, for June 2013 with induced precipitation wherein a considerable band of low frequency rays can be seen to reach northern Russia; the rays provided coverage out to a bearing exceeding the ± 45° azimuthal field of view (FOV) of the model OTHR, implying that horizontal deviations from great circle propagation occurred. This was attributed to the auroral side scattering of low frequency rays as they underwent refraction by the edge of the auroral oval; the auroral oval directly intersects the great circle path at the edge of the FOV. The introduction of non-great-circle (NGC) propagation modes are expected to have profound implications for the reliability of OTHR target detection as the complexities of accurately positioning an uncooperative target will be significantly furthered given that great-circle propagation cannot be assumed in all cases. NGC modes are expected to introduce uncertainties to both range and direction as radio waves may be received from unexpected directions with significant time delays due to the increased path length. This presents key difficulties for designing a reliable target coordinate registration system (TCRS) for a mono- or bi-static OTHR; however, including an increased number of receive arrays spread laterally over a large area could potentially alleviate NGC errors due to the additional receive perspectives aiding positioning.

The extreme ranges seen to exceed 5,000 km in many cases appear at first observation to be beneficial to radar performance; however, these ranges are not practical for OTHR as the considerable path losses result in low power radar returns that may not be discernible from clutter due to inadequate equipment sensitivity. In addition to being difficult to detect, the coverage provided by these rays was highly variable in terms of AE index and time, with the covered area limited to only small regions. Because of this, the long-distance propagating

rays would likely act as a detrimental source of additional clutter to the OTHR system.

The strength of the F-region was attributed as the most important factor influencing auroral effects on coverage and is directly linked to climatological conditions; F-region plasma density relies heavily on solar activity, time of day, and season. This is crucial because without a strong F-region, F-E ducted propagation is unavailable, as insufficient NmF2 ionisation prohibits the refraction of ducted rays. As a result, auroral propagation is restricted to Auroral E-mode at close ranges, implicating that coverage beyond ~1800 km is unattainable. The cases of April and January during both years tested demonstrated this limitation as a result of reduced photoionisation, due to seasonal and solar cycle variations. This decrease in range is also expected from the storm response of NmF2, wherein a deteriation occurs in NmF2 at these latitudes during storms over the course of hours to days, as seen in E-CHAIM's Storm NmF2 submodel. The reader may wish to consult Themens et al. (2018) for a full explanation of E-CHAIM's storm pertubation model; however, the model mainly captures the decrease in ionospheric electron density on daily timescales that occurs during storms at high latitudes as a result of a relative increase recombination (Themens et al., 2020). This relative increase in reccombination ratecan result in a reduction to the plasma density by a factor of up to 2 in the F-Region (Riddolls, 2006). The small band of low frequency F-E ducted mode rays between 2,000- and 3,000-km in Figure 10A show some increase in coverage density as the ionosphere recovers from the storm however, this is only a minor observation as the mode is difficult to discern. Despite the minor difference, it is worth noting that the F-E mode could be restricted in this manner. Storm effects on auroral propagation may be more profound given different combinations of storm and precipitation intensities, although the two are often linked. The effects shown within the casestudy demonstrate the radar during a significant solar weather event and so, frequency availability is expected to be similar to Figure 10C for quiter conditions.

The observed increase in maximum frequency with aurora is beneficial as it permits potentially greater radar returns from smaller targets; this is because the smaller wavelength relative to the size of the target places the radar cross section (RCS) within the resonant region, acting to improve detection by increasing target returned power (Knott, Shaeffer, & Tuley, 2004). For example, a 26 MHz ray has a wavelength of 11.53 m, comparable to small aircraft. An interested reader may consult Knott et al. (2004) for a further description of factors affecting target RCS. This is problematic as without aurora, only low frequencies are supported at night, suggesting that the OTHR would be susceptible to small targets penetrating the surveillance area without detection due to a low RCS.

Within this paper, a large elevation range of 1°-60° was explored and it is worth noting that despite raytracing determining low elevation rays as coverage, much of this propagation is unlikely to be suitable. OTHR antennas are usually unable to reach elevations below ~5° without facing a significant reduction in gain and

this is demonstrated in Cervera's (2018) array model. This considerably limits power output at such elevations, reducing the probability of detection. Despite this, the data produced using the methodology employed herein can be filtered to extract a specific frequency or elevation range to suit a more tightly defined radar array.

Further study, using existing HF radar systems, such as the Super Dual Auroral Radar Network (SuperDARN), will be conducted in subsequent work to further test the results herein and to validate the raytracing models used.

# Conclusions

Auroral structures present within the high latitude ionosphere are problematic for OTHR as the propagation environment must be well understood to ensure reliable operation; to this end, HF propagation modelling is invaluable for OTHR success. Within this study, a suitable HF propagation model has been demonstrated to assess auroral variations in frequency coverage for a hypothetical OTHR. A high sensitivity to auroral intensity was observed for coverage, with a considerable dependence to climatological conditions due to reliance on the F-region. In addition to this, the storm time dependency of Auroral F-E ducted propagation was noted. Aurora have been shown to increase MUF by up to 17.5 MHz and introduce two additional night-time propagation modes: Auroral E-mode and F-E ducted mode. A reduction in median range of up to 1,315 km was observed with aurora. A transition stage was identified as auroral modes become active with increasing AE index. Ducted propagation enabled long distance propagation of rays along the auroral oval and in some cases, NGC propagation was introduced by aurora. Low frequency rays dominated OTHR coverage, except for in small regions when aurora were present, wherein a MUF of 26 MHz was often supported; this made evident the necessity for high latitude OTHR systems to deploy both a low- and high-band array to ensure aurora tolerance. The range and sensitivity of feasible operating parameters presented within this study demonstrate that utilising an FMS and TCRS capable of accounting for the highly volatile ionospheric conditions is paramount to the successful operation of high latitude systems.

# Acknowledgements

The results published in this paper were obtained using the HF propagation toolbox, PHaRLAP, created by Dr Manuel Cervera, Defence Science and Technology Group, Australia (`manuel.cervera@dst.defence.gov.au`). Version 4.4.2 of Pharlap was used within this study. This toolbox is available from https://www.dst.defence.gov.au/opportunity/pharlap-provision-high-frequency-raytracing-laboratory-propagation-studies. E-CHAIM version 3.2 was used for this study. Source codes for E-CHAIM can be acquired at https://e-chaim.chain-project.net/. We acknowledge the support of the Canadian

Space Agency (CSA) under grant 21SUSTCHAI. F10.7 flux data used in this study is produced by the National Research Council Canada in partnership with Natural Resources Canada and can be accessed from https://www.spaceweather.gc.ca/forecast-prevision/solar-solaire/solarflux/sx-en.php. The Kp index is from the GFZ Helmholtz Centre Potsdam and can be accessed at https://www.gfz-potsdam.de/en/kp-index/. AE index data included in this study is taken from the World Data Centre for Geomagnetism Kyoto, available at http://wdc.kugi.kyoto-u.ac.jp/aedir/.

# References

Bates, H. F., Albee, P. R., and Hunsucker, R. D. (1966), On the relationship of the aurora to non-great-circle high-frequency propagation, J. Geophys. Res., 71( 5), 1413– 1420, doi:10.1029/JZ071i005p01413.

Bjoland, L. M., Belyey, V., LØvhaug, U. P., & Hoz, C. L. (2016). An evaluation of International Reference Ionosphere electron density in the polar cap and cusp using EISCAT Svalbard radar measurements. Annales geophysicae, 34, 751-758. https://doi.org/10.5194/angeo-34-751-2016

Cameron, A. (1995). The Jindalee Operational Radar Network: Its Architecture and Surveillance Capability. Proceedings International Radar Conference, 1995, pp. 692-697, doi: 10.1109/RADAR.1995.522633.

Cervera, M. A., & Harris, T. J. (2014). Modeling ionospheric disturbance features in quasi-vertically incident ionograms using 3-D magnetoionic ray tracing and atmospheric gravity waves. Journal of Geophysical Research: Space Physics, 119, 431-440. https://doi.org/10.1002/2013JA019247

Cervera, M. A., Francis, D. B., & Frazer, G. J. (2018). Climatological model of over-the-horizon radar. Radio Science, 53, 988– 1001. https://doi.org/10.1029/2018RS006607

Chengyu, H., Guo, K., & Yili, F. (2015). The sky-wave radar detection performance computing based on the dynamic ionospheric model. Neurocomputing 151, 1305-1315. https://doi.org/10.1016/j.neucom.2014.10.073

Croft, Thomas A., (1967), Computation of HF Ground Backscatter Amplitude, Radio Science, 2, doi: 10.1002/rds196727739. Davies, K. (1965). Ionospheric Radio Propagation. Washington, D.C.: U.S. Department of Commerce.

Doerry, A. W. (2013). Earth Curvature and Atmospheric Refraction Effects on Radar Signal Propagation. Sandia National Laboratories. Report: SAND2012-10690. Retrieved from: https://www.researchgate.net/publication/277011644_Earth_Curvature_and_Atmos

Fowle, E. N., Key, E. L., Millar, R. I., & Sear, R. (1979). The Enigma of the AN/FPS-95 OTH Radar. Beford, Mass.: The Mitre Corporation.

Francis, D. B., Cervera, M. A., & Frazer, G. J. (2017). Performance Prediction

for Design of a Network of Skywave Over-the-Horizon Radars. IEEE A&E Systems Magazine, 18-28. https://doi.org/10.1109/MAES.2017.170056

Haselgrove, C., & Haselgrove, J. (1960). Twisted Ray Paths in the Ionosphere. Proceedings of the Physical Society (1958-1967), 75, pp. 357-363. https://doi.org/10.1088/0370-1328/75/3/304

Haselgrove, J. (1963). The Hamiltonian Ray Path Equations. Journal of Atmospheric and Terrestrial Physics, 25(7), 397-399. https://doi.org/10.1016/0021-9169(63)90173-9

Hunsucker, R. D., & Bates, H. F. (1969). Survey of polar and auroral region effects on HF propagation. Radio Science, 4(4), 347-365. https://doi.org/10.1029/RS004i004p00347

Jones, R., & Stephenson, J. (1975). A Versatile Three-Dimensional Ray Tracing Computer Program for Radio Waves in the Ionosphere. NASA STI/Recon Technical Report.

Knott, E. F., Shaeffer, J. F., & Tuley, M. T. (2004). Radar Cross Section (2nd Edition). SciTech Publishing. Retrieved from https://app.knovel.com/hotlink/toc/id:kpRCSE0001/radar-cross-section-2nd/radar-cross-section-2nd

Lockheed-Martin. (2021). TPS-77 Specification Brochure. Retrieved 12 2020, 17, from Lockheed-Martin: https://www.lockheedmartin.com/content/dam/lockheed-martin/rms/documents/ground-based-airsurveillance-

Mingalev, I.V., Suvorova, Z.V., Shubin, V.N. et al. (2021) Differences in the Predicted Conditions of Shortwave Radio Communication between a Medium-Latitude Transmitter and a Receiver in the Arctic Region with the Use of Different Empirical Ionospheric Models. Geomagn. Aeron. 61, 565–577. https://doi-org.proxy.hil.unb.ca/10.1134/S0016793221040095

Nengye Liu, E. A. (2017). The European Union and the Arctic. Boston: Brill. Retrieved from http://www.jstor.org/stable/10.1163/j.ctt1w8h3gv.6

Ponsford, A. M. (2015). Canada's Third Generation High Frequency Surface Wave Radar (HFSWR) System for Persistent Surveillance of the EEZ. Raytheon Canada Limited. https://doi.org/10.13140/RG.2.1.1307.5605

Riddolls, R. J. (2006). A Canadian Perspective on High-Frequency Over-the-Horizon Radar. Ottawa: Defence Research and Development Canada.

Rogers, N. C., Warrington, E. M., & Jones, T. B. (2003). Oblique ionogram features associated with off-great circle HF propagation at high and sub-auroral latitudes. IEE Proceedings - Microwaves Antennas and Propagation, 150(4), 295-300. doi: 10.1049/ip-map:20030552

Settimi, A., & Bianchi, S. (2014). Ray Theory Formulation and Ray Tracing Method. Ray Theory Formulation and Ray Tracing Method. Quaderni di Geofisica, Istituto Nazionale di Geofisica e Vulcanologia, https://www.earth-prints.org/bitstream/2122/9139/1/quaderno121.pdf

Smith, N., (1939), The Relation of Radio Sky-Wave Transmission to Ionosphere Measurements, Proceedings of the IRE, vol. 27, no. 5, pp. 332-347, doi: 10.1109/JRPROC.1939.228397

Thayaparan, T., Dupont, D., Ibrahim, Y., & Riddolls, R. (2019). Extracting Radar Parameters for Sky-Wave Over-The-Horizon Radar using Ray-Tracing through a Model of Ionosphere. Ottawa: Defence Research and Development Canada. Retrieved 01 2021, 03, from https://cradpdf.drdc-rddc.gc.ca/PDFS/unc342/p811300_A1b.pdf

Thayaparan, T., Ibrahim, Y., Polak, J., & Riddolls, R. (2018). High-Frequency Over-the-Horizon Radar in Canada. IEEE Geoscience and Remote Sensing Letters, 15(11), 1700-1704. https://doi.org/10.1109/LGRS.2018.2856185

Thayaparan, T., Marchioni, J., Kelsall, A., & Riddolls, R. (2020). Improved Frequency Monitoring System for Sky-Wave Over-the-Horizon Radar in Canada. IEEE Geoscience and Remote Sensing Letters, 17(4), 606-610. https://doi.org/10.1109/LGRS.2019.2928172

Thayaparan, T., Riddolls, R., & Shimotakahara, K. (2016). Frequency Monitoring System for Over-the-Horizon Radar (OTHR) in Canada. 2016 17th International Radar Symposium (IRS) (pp. 1-5). Crown. https://doi.org/10.1109/IRS.2016.7497370

Themens, D. R., P.T. Jayachandran, M.J. Nicolls, and J.W. MacDougall (2014), A top to bottom evaluation of IRI 2007 within the polar cap, J. Geophys. Res. Space Physics, 119, 6689–6703, doi:10.1002/2014JA020052.

Themens, D. R., & Jayachandran, P. T. (2016). Solar activity variability in the IRI at high latitudes: Comparisons with GPS total electron content. Journal of Geophypsical Research: Space Physics, 121, 3793-3807, https://doi.org/10.1002/2016JA022664.

Themens, D. R., Jayachandran, P. T., Galkin, I., & Hall, C. (2017). The Empirical Canadian High Arctic Ionospheric Model (E-CHAIM): NmF2 and hmF2. Journal of Geophysical Research: Space Physics. https://doi.org/10.1002/2017JA024398.

Themens, D. R., Jayachandran, P. T., Reid, B., McCaffrey, A. M. (2018). The Limits of Empirical Electron Density Modeling: Examining the Capacity of E-CHAIM and the IRI for Modeling Intermediate (1- to 30-Day) Timescales at High Latitudes. Radio Science, 54. https://doi.org/10.1029/2018RS006763

Themens D. R., Jayachandran, P. T. & McCaffrey, A. M. (2019a). Validating the performance of the Empirical Canadian High Arctic Ionospheric Model (E-CHAIM) with in situ observations from DMSP and CHAMP. J. Space Weather Space Clim. 9, A21. https://doi.org/10.1051/swsc/2019021

Themens, D. R., Jayachandran, P. T., McCaffrey, A. M., Reid, B., & Varney, R. H. (2019b). A bottomside parameterization for the Empirical

Canadian High Arctic Ionospheric Model. Radio Science, 54, 397–414. https://doi.org/10.1029/2018RS006748

Themens, D. R., Watson, C., McCaffrey, A., Reid, B., & Jayachandran, P. (2020). The Development and Implementation of a Precipitation Enhanced E-Region for E-CHAIM. Ottawa: Report submitted to Defence Research and Development Canada for contract #W7714-186507/001/SS (public release TBD).

Watson, C., D.R. Themens, and P.T. Jayachandran (2021), Development and Validation of Precipitation Enhanced Densities for the Empirical Canadian High Arctic Ionospheric Model (E-CHAIM). *Space Weather* (Accepted, Manuscript # 2021SW002779RR)

**Figure Captions**

Figure . Map showing the location of the hypothetical OTHR with reference range markings in red, with comparison to the maximum range of a co-located Lockheed-Martin TPS-77 long-range radar in green. The anticipated range of the OTHR is seen to cover a large sector of the Arctic. 360° coverage is not envisioned for this radar however, the range markings suggest notional range for all boresight angles.

Figure . Vertical electron density profile at 65°N 0°W within the auroral zone showing the E-CHAIM sub-models for 15th July 2010 at 00 UT. A pronounced E-region enhancement introduced by an artificial aurora with an AE index of 500 nT is clear at an altitude of ~110 km. The D-region sub-model is active for each of the profiles but has no effect.

Figure . Electron density distribution at 102.5km altitude for A) low solar activity (2010) and B) high solar activity (2013) showing dayside and auroral enhancements to the E-region. Note the clear auroral oval for cases with precipitation. The D-region, Storm and Precipitation models were active in each plot.

Figure 4. Frequency coverage for A) low solar activity (2010) and B) high solar activity (2013) for each case outlined in Table 1 at a target altitude of 10 km for both precipitation OFF, and aurora induced with AE index set to 500 nT. The E-CHAIM storm and D-region models were active for all subplots.

Figure 5. 2D NRT propagation cross section plots for the model OTHR under different conditions and frequencies on the 16th of June 2013 showing in: A) the F-region of the ionosphere acting as an ideal reflector with no precipitation active; B) the three propagation modes present with aurora providing different bands of ranges; C) long range ducted propagation along the auroral oval at a bearing of 35° from boresight. The Storm and D-region sub models of E-CHAIM are active in each.

Figure 6. Propagation sensitivity presented by range versus AE index with a frequency colourmap for 6 climatological conditions. Note the transition at 50 nT.

Figure 7. 2D NRT cross section for the model OTHR at boresight for April 2013 with AE set to 500 nT, showing long range propagation of rays skimming the reference altitude.

Figure 8. Map showing flightpaths A and B in red and green, respectively. The radar location is marked by a blue cross with boresight and azimuthal field of view shown with red dashed lines.

Figure 9. Frequency coverage for flightpath A and B, showing an increase in MUF and range with artificial aurora. In both subplots A and B, the azimuthal extent of the OTHR field of view is marked by a red dashed line, making clear that nominal coverage exceeds 100% in some cases. In subplot A, the mode transition from Auroral E-mode to E-F ducted propagation is signified by the drop in frequency at a distance approximately 75% along the path and is highlighted by a blue dashed line. For subplot B, no target coverage is seen for three cases without precipitation. Note that the E-CHAIM storm and D-region models were active for all flightpath analysis.

Figure 10. Variation in frequency and ground range with time during the peak of the 2010 May geomagnetic storm with different combinations of the E-CHAIM precipitation and storm sub models active. The 2D NRT is performed for the hypothetical OTHR at boresight. Note that a log scale is used to represent frequency in the colormap. Subplot A represents the optimal setup of E-CHAIM for auroral conditions due to consideration of both precipitation and storm effects. The inclusion of subplot B directly shows the resulting propagation environment with auroral ionisation removed, effectively making clear the effect of precipitation when compared to A. Quiet conditions are represented in subplot C by the removal of both ionospheric effects. AE index data is included for comprehension of geomagnetic conditions in subplot D. Red and black dashed lines in subplot A indicate the nominal maximum nighttime range prior to and during the storm with induced precipitation, respectively.